Boise State University
ScholarWorks

Mechanical and Biomedical Engineering Faculty Publications and Presentations

Department of Mechanical and Biomedical Engineering

1-1-2018

Waste Heat Recovery from Distributed Rack-Based Fuel Cells Using Thermoelectric Generators

Khosrow Ebrahimi
Boise State University

Alfonso Ortega
Santa Clara University

Calvin Li
Villanova University

Kazuaki Yazawa
Purdue University

Sean James
Microsoft, Inc.

© 2018 IEEE. Personal use of this material is permitted. Permission from IEEE must be obtained for all other uses, in any current or future media, including reprinting/republishing this material for advertising or promotional purposes, creating new collective works, for resale or redistribution to servers or lists, or reuse of any copyrighted component of this work in other works. doi: 10.1109/ITHERM.2018.8419483

This is an author-produced, peer-reviewed version of this article. The final, definitive version of this document can be found online at *Proceedings of the Seventeenth InterSociety Conference on Thermal and Thermomechanical Phenomena in Electronic Systems: Itherm 2018*, published by IEEE. Copyright restrictions may apply. doi: 10.1109/ITHERM.2018.8419483

Waste Heat Recovery from Distributed Rack-Based Fuel Cells Using Thermoelectric Generators

Khosrow Ebrahimi
Department of Mechanical and Biomedical Engineering
Boise State University
Boise, Idaho, USA, 83706
Email: khosrowebrahimi@boisestate.edu

Alfonso Ortega
School of Engineering
Santa Clara University
Santa Clara, California, USA, 95053
Email: alortega@scu.edu

Calvin Li
Department of Mechanical Engineering
Villanova, Pennsylvania, USA, 19085
Email: calvin.li@villanova.edu

Kazauki Yazawa
Birck Nanotechnology Center
Purdue University
West Lafayette, Indiana, USA, 47906
Email: kyazawa@purdue.edu

Sean James
Microsoft, Inc.
Redmond, Washington, USA, 98052
Email: Sean.James@microsoft.com

ABSTRACT

Off-grid power generation has been demonstrated in data centers through the deployment of site-specific centralized power plants utilizing gas turbine or fuel cell-based power generation. Because power is centrally generated, power distribution requires a high voltage power grid within the data center with its ancillary storage and conditioning requirements and equipment. An alternative approach is a completely decentralized distributed power generation system in which fuel cells deployed within individual server racks provide power localized to that rack only. Among other advantages, such an approach also greatly increases the ability to modulate and control power to individual rack units. Because the Solid Oxide Fuel Cells (SOFC) proposed in this approach are air-cooled and have extremely high air exhaust temperatures, of order 800 ^{o}C, the optimal energy efficient design of an overall localized fuel-cell power generation system should also consider the opportunities to recover and re-use the waste heat. This paper reports on the development of a coupled thermal-electrical model of a thermoelectric generator (TEG) based energy recovery system operating between the fuel cell hot exhaust air temperature and a warm water cooling system deployed within the rack for server cooling. The power generation system consisted of a TEG module sandwiched between a hot air heat exchanger and a colder water based heat exchanger. The design of the TEG module for maximum power generation is heavily coupled with thermal and electrical conditions. Distribution of temperature on generator surfaces change the optimum design, hence the optimization of generator system required co-optimization with the design of the heat exchangers. This paper will present the results of a co-optimization study considering the effects of thermal parameters such as exhaust gas mass-flow-rate and temperature, cooling water volumetric-flow-rate and temperature, hot- and cold-flow parallel and counter-flow arrangements, as well as the thermal-electrical considerations in the TEG design including the design of the Thermo-Electric junctions, fractional area coverage of thermoelectric elements, and substrate thickness.

KEY WORDS: waste heat recovery, server rack, cooling water, fuel cell, TEG module, thermoelectric model

NOMENCLATURE

A	area/ total surface area, m^2
Bi	Biot number
D	channel diameter, m
c_p	specific heat capacity at constant pressure, kJ/kg K
d_{el}	electrode thickness, m
F	TED module filling factor
H	height/ height of the fin, m
h	convection heat transfer coefficient, kW/m^{2}K
k	thermal conductivity of the base of heat-sink or cold-

This is an author-produced, peer-reviewed version of this article. The final, definitive version of this document can be found online at *Proceedings of the Seventeenth InterSociety Conference on Thermal and Thermomechanical Phenomena in Electronic Systems: Itherm 2018*, published by IEEE. Copyright restrictions may apply. doi: 10.1109/ITHERM.2018.8419483

	plate, kW/m K
L	length of rack floor area, m
λ	characteristic length, m
M	molar mass, g/mol
m	fin parameter, 1/m
m	electrical resistance ratio
$\dot{m}$	mass-flow-rate, kg/s
mf	mass fraction
N	number of TEG/heat-sink/cold-plate rows or columns
N	number of semiconductor elements per unit area
$N_{TEG\text{-}Rack}$	number of server racks equipped with TEG modules
NTU	number of transfer units
Nu	Nusselt number
n	number of moles
Pr	Prandtl number
Q	volumetric-flow-rate, m^3/s, GPM
Re	Reynolds number
R, R_{th}	thermal resistance, K/W
RU, U	rack unit= 44.45 mm=1.75 in
S	Seebeck coefficient = $2.4(10^{-4})$ V/K
T	temperature, ^oC and K
t	fin thickness, m
U	flow velocity, m/s
W	width of rack floor area, m
x	distance from the inlet of the duct, m
x*	dimensionless distance from the inlet of the duct
y	molar fraction
Z	figure of merit of TE material

Greek symbols

ε	effectiveness of heat-sink or cold-plate
ε	emissivity
σ	electrical conductivity of semiconductor legs, 1/S/m
σ_{el}	electrical conductivity of electrodes, 1/S/m
η_O	overall surface efficiency
ρ	mass density, kg/m^3
ρ_{ec}	specific contact resistivity ($=10^{-6}\Omega.cm^2$)
ν	kinematic viscosity, m^2/s
μ	dynamic viscosity, Pa.s
$\bar{\upsilon}$	molar specific volume, m^3/mol
Ψ	internal/resultant thermal resistance, Km^2/W

Subscripts

b	base of the heat-sink or cold-plate
C	column
CP	cold-plate
c	TEG cold side
ch	channel
cond	conduction
cont	contact
rad	radition
D_h	calculated based on the hydraulic diameter
e	entrance region
exhaust	fuel cell exhaust gas
f	fin
fluid	hot or cold fluid
gap	TEG module gap fill material (which is air)
g	gas
h	hydraulic
h	TEG hot side
HS	heat-sink
i, j	constituents of mixture
leg	TEG semiconductor legs
Mix	mixture
R	row
s, sub	substrate
TEG	thermoelectric generator
TIM	thermal interface material
W	water

Superscripts

*	calculated based on x*

INTRODUCTION

Thermoelectric generation is a technology to directly convert waste heat into electricity. Thermoelectric Generators (TEGs) operate based on a phenomenon known as the Seebek effect [1]. According to the Seebeck effect, when two different materials with different conduction energy band levels (such as semiconductors) are subjected to a temperature difference, a voltage is created. For waste heat energy capture, the hot side of TEG is coupled to a waste heat source and because of the high temperature difference between cold and hot sides of TEG, a voltage is generated. The energy absorbed at the TEG junction provides enough additional energy to bridge the energy gap between the N- and P-type semiconductor pellets and initiate electrical flow. In this way thermal energy is directly converted into electrical energy [1].

In the conceptual waste heat recovery configuration, as shown in Fig. 1, the waste heat source is the Solid Oxide Fuel Cell (SOFC) exhaust gas. The temperature of the exhaust gas can be as high as 780^{o}C [2]. The SOFC fuel cell power modules are deployed within individual server racks in a water-cooled data center. A shelf of each server rack is carpeted by TEG modules (see Figs. 1-3). Two ducts are provided on the top and bottom sides of the TEG modules shelf. While the fuel cell exhaust gas is conducted through the lower duct, the warm water exiting the cooling circuit of the servers, placed in the same rack, is manages to pass through the upper duct before conducted toward the water chiller (see Fig. 1). Optimized heat sinks are designed to extract the maximum possible heat energy from the hot gas flowing over the TEG modules in the lower duct (see Fig. 2). Also, optimal cold plates are designed to extract the maximum possible heat energy from the cold side of the TEG modules in the upper duct in order to guarantee the maximum temperature difference between hot and cold sides of the TEG modules (see Fig. 2). A model is developed to assess the effectiveness of this waste heat recovery configuration through laying out the specifications of the optimized heat sink and cold plate based on the thermal operating conditions of the system. The sensitivity of the performance of this configuration to the specifications of TEG modules is studied using the developed analytical model.

This is an author-produced, peer-reviewed version of this article. The final, definitive version of this document can be found online at *Proceedings of the Seventeenth InterSociety Conference on Thermal and Thermomechanical Phenomena in Electronic Systems: Itherm 2018*, published by IEEE. Copyright restrictions may apply. doi: 10.1109/ITHERM.2018.8419483

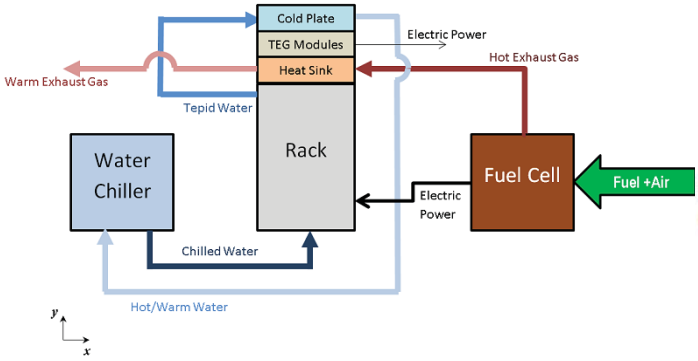

Fig. 1 Schematic of conceptual integration of fuel cell and TEG modules (in counter flow) configuration.

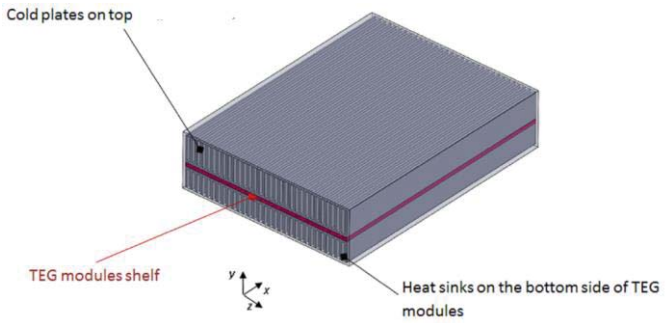

(a) 3D view

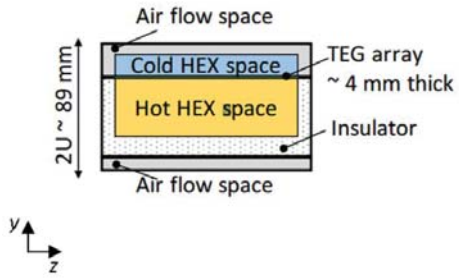

(b) Front view[1]

Fig. 2 3D and front schematic views of the rack shelf carpeted by TEG modules. The hot SOFC exhaust gas passes through the heat sinks underneath the TEG modules and the water exiting the rack cooling cycle flows through the cold plates on top of the TEG modules.

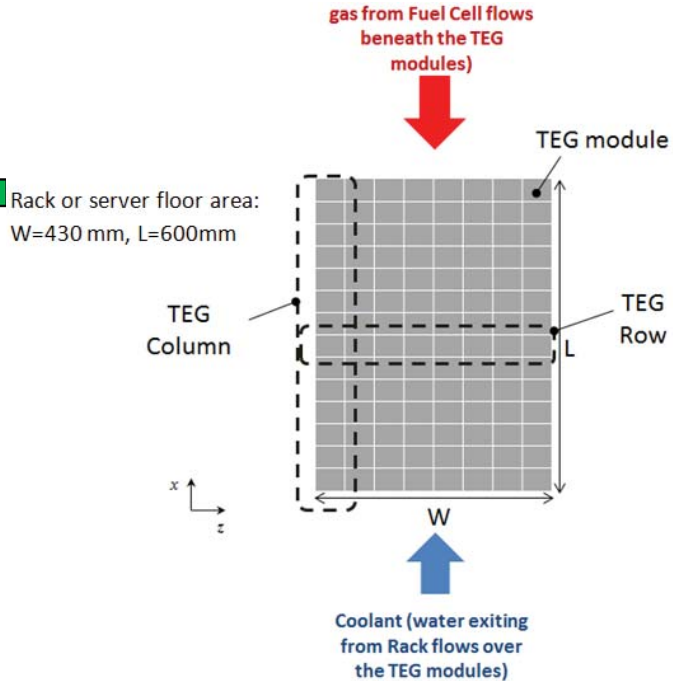

Fig. 3 Top view of shelf rack floor area carpeted by TEG modules. The rows and columns of TEG modules are shown. The directions of hot and cold streams are for counter-flow configuration.

MODEL DEVELOPMENT: ASSUMPTIONS AND APPROACH

The following assumptions are taken into account in developing the model:

1. The waste heat source is the exhaust gas of a 220 kW SOFC fuel cell [2]. This amount of power supplied enough energy for the operation of ~14.6 server racks of 15kW. The mass flow rate and temperature of the exhaust gas at the outlet of the fuel cell are 0.502kg/s and 780 ^{o}C, respectively.
2. All the fuel cell-powered server racks are equipped with a shelf of TEG modules.
3. The exhaust gas mass flow rate is equally divided between all the fuel cell-powered server racks.
4. The fuel cell exhaust gas is assumed to be an ideal mixture of CO_2 and H_2O.
5. The cold stream which removes the heat from the cold side of TEG modules is provided by the water-cooled server racks. The cooling water exiting the server rack passes through the cold plates mounted on the cold side of TEG modules, on its path towards the chiller.
6. The volumetric flow rate of cooling water in each rack of 15 kW is 5 GPM. The volumetric flow rate of cooling water in a typical water cooled server rack of 13-26 kW is in the range of 5-10 GPM [3].
7. The temperature of water at the exit of each server rack and the inlet of the cold stream duct attached to the top side of the TEG array shelf is in the range of 22 ^{o}C-80 ^{o}C [3].

[1] Image by K.Yazawa, Purdue University

This is an author-produced, peer-reviewed version of this article. The final, definitive version of this document can be found online at *Proceedings of the Seventeenth InterSociety Conference on Thermal and Thermomechanical Phenomena in Electronic Systems: Itherm 2018*, published by IEEE. Copyright restrictions may apply. doi:10.1109/ITHERM.2018.8419483

8. Averaged properties of P-type and N-type semiconductors are considered as the properties of thermoelectric (TE) elements (legs).
9. Due to the very high thermal conductivity and very thin thickness, the thermal resistance of TE electrodes is negligible.
10. Each TEG module is assumed to have the dimensions of 1 in x 1 in.
11. Every Heat sink and cold plate has the same base area as the TEG module. Therefore, the number of heat sinks and cold plate are equal to the number of TEG modules.
12. High performance thermal compound with thermal conductivity of 1.18 W/m/K is selected as Thermal Interface Material (TIM). The thickness of TIM is assumed to be 0.002 in [4].
13. The server rack floor area is assumed to have dimensions of 430 mm x 600 mm.

Our approach is based on developing optimized designs for the heat sink and the cold plate, and then calculation of the optimum TE element (TE leg) thickness at which the thermoelectric power output reaches to its maximum amount. To calculate the optimum TE element thickness, the TEG external resistances should be determined first [5]. The external thermal resistance in the hot side is the resultant of thermal resistances of heat sink, TIM and hot side substrate of the TEG module. In the cold side, the external thermal resistance is the resultant of thermal resistances of cold plate, TIM and cold side substrate of the TEG module. The design optimization for heat sink and cold plate is performed to achieve the highest possible effectiveness based on the thermal and flow conditions of the exhaust gas and cooling water at the inlet of the TEG modules shelf.

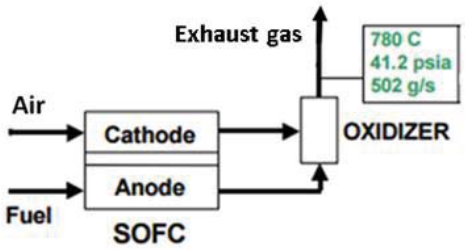

Fig. 4 Thermal conditions of the exhaust gas at the exit of 220 kW SOFC [2].

In overall, after the design optimization of the heat sink and cold plate, the algorithm introduced by Yazawa et al. [5, 6] (see Fig. 5), is deployed to develop the thermal and electrical modeling as well as optimization of TEG module design and operating conditions. To start the calculations, the baseline values of TEG properties, listed in Table 1, along with the temperate and flow rate of the hot and cold streams at the inlet of the TEG modules shelf are considered as input parameters.

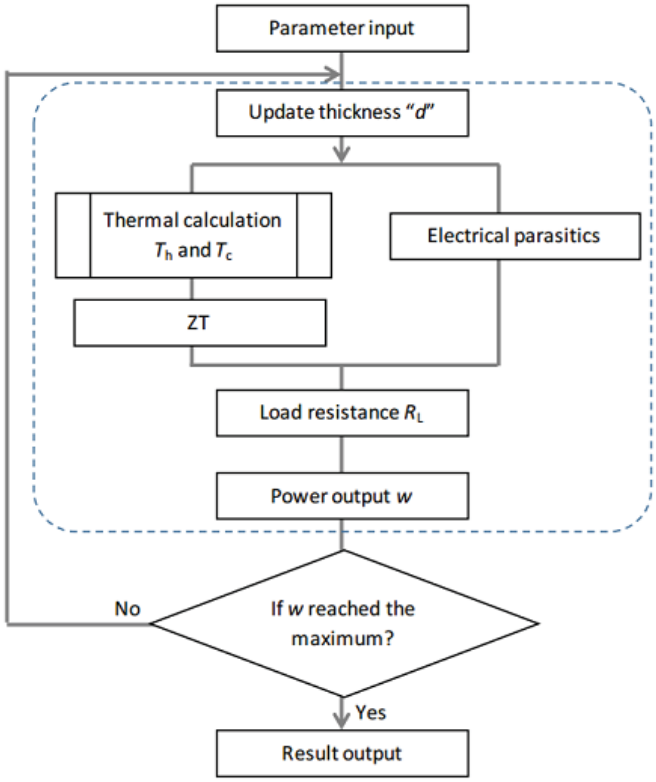

Fig. 5 The flowchart of the algorithm used for Thermoelectric model development [5, 6].

Heat Sink and Cold Plate Design Optimization

For every TEG module in the TEG array shelf, a heat sink and a cold plate are required to attach to the hot and cold sides of TEG module. Therefore, the number of heat sinks and cold plates are equal to the number of TEG modules. It is assumed that heat sink design specifications are the same for all TEG modules. Similar assumption is also considered for the cold plates. Design optimization for the heat sink and cold plate are performed based on the exhaust gas and the cooling water thermal conditions at the inlet of the ducts attached to the hot and cold sides of the TEG array shelf. Heat sinks and cold plates have the same base area as the TEG module and similar to TEG modules they are arrayed in rows and columns which cover both sides of TEG modules (see Figs 3 and 6).

Knowing the dimensions of the rack floor area and TEG module, the number of TEG/heat sink/cold plate rows and columns (see Fig. 3) are calculated as below

$$N_R = \left\lfloor \frac{L}{L_{TEG}} \right\rfloor \quad (1)$$

$$N_C = \left\lfloor \frac{W}{W_{TEG}} \right\rfloor \quad (2)$$

This is an author-produced, peer-reviewed version of this article. The final, definitive version of this document can be found online at *Proceedings of the Seventeenth InterSociety Conference on Thermal and Thermomechanical Phenomena in Electronic Systems: Itherm 2018*, published by IEEE. Copyright restrictions may apply. doi:10.1109/ITHERM.2018.8419483

Table 1. The baseline values of TEG properties

Parameter	Baseline value
Number of semiconductor elements (TEG legs) per unit area, N	$10^6/m^2$
TEG module filling factor, F	0.3
TE leg thickness, d	6×10^{-4}m
Thermal conductivity of semiconductor legs, k_{leg}	1.5 W/m/K
Thermal conductivity of gap fill material (air), k_{gap}	0.026/W/m/K
Electrical conductivity of semiconductor legs, σ	$8x10^4$ 1/S/m
Seebeck coefficient, S	2.4×10^{-4}V/K
Substrate (Al_2O_3) conductivity, k_s	20 W/m/K
Substrate emissivity, ε_s	0.2
Substrate thickness, t_s	10^{-3} m
Electrode thickness, d_{el}	50×10^{-6} m
Thermal conductivity of electrodes (Copper), k_{el}	400 W/m/K
Electrical conductivity of electrodes, σ_{el}	$6\times10^7$1/S/m
Specific contact resistivity, ρ_{ec}	$10^{-6}\Omega.cm^2$

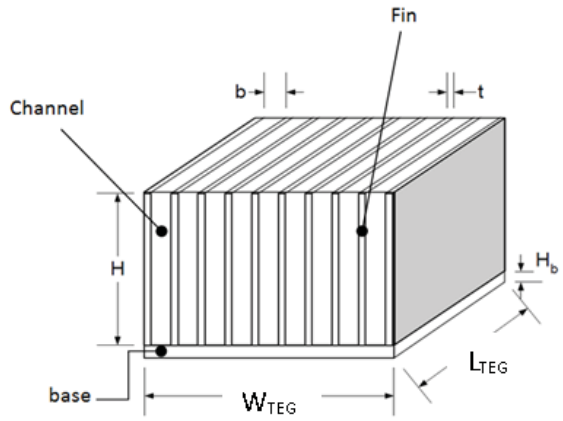

Fig. 6 Heat Sink/Cold Plate dimensions [7].

The approach of design optimization for heat sink and cold plate is based on assuming fixing values for fin thickness, fin height and base height (as indicated in Table 2) and then calculating the optimal value of either fin spacing or the number of fins when the objective function is the heat sink/cold plate thermal resistance:

$$R_{th} = \frac{1}{\dot{m}_C c_{p_{fluid}} \varepsilon} + \frac{H_b}{k.A_b} \quad (3)$$

where ε is the heat sink or cold plate effectiveness. $\dot{m}_C$ is the mass flow rate of the hot or cold stream through one column of heat sinks or cold plates attached to the bottom or top side of TEG column (see Fig. 3). c_{pfluid} is the heat capacity of hot or cold fluids. k is the thermal conductivity of the heat sink/cold plate base. A_b and H_b are the base area and the base height of the heat sink/cold plate, respectively.

Calculation of heat sink/cold plate effectiveness. The heat sink or cold plate effectiveness is calculated through the following equation [7]

$$\varepsilon = 1 - e^{-\eta_O.NTU} \quad (4)$$

In the equation above, η_o and NTU denote the overall surface efficiency and Number of Transfer Units, respectively and calculated as below [8]

$$\eta_O = 1 - \frac{A_f}{A}(1-\eta_f) \quad (5)$$

$$NTU = \frac{h.A}{\dot{m}_C.c_P} \quad (6)$$

The entire fin surface area (A_f) and the total surface area (A), in the right-hand- side (RHS) of Eqs. (5) and (6), are calculated as below

$$A_f = 2(N_f - 1).H.L_{TEG} \quad (7)$$

$$A = 2(N_f - 1).H.L_{TEG} + 2(N_f - 1).b.L_{TEG} \quad (8)$$

The fin efficiency (η_f), in the RHS of Eq. (5), is calculated using Eqs. (9) and (10) [8].

$$\eta_f = \frac{\tanh(mH)}{mH} \quad (9)$$

where m is the fin parameter,

$$m = \sqrt{\frac{2h}{k.t}} \quad (10)$$

In the calculation of the convection heat transfer coefficient (h), in the RHS of Eqs. (6) and (10), a couple of Nusselt (Nu) correlations are examined based on the channel hydraulic entrance length. As it is seen in Fig.6, the channel is defined as the space between two consecutives parallel plate fins. The channel hydraulic entrance length is estimated through the following correlations [9]

This is an author-produced, peer-reviewed version of this article. The final, definitive version of this document can be found online at *Proceedings of the Seventeenth InterSociety Conference on Thermal and Thermomechanical Phenomena in Electronic Systems: Itherm 2018*, published by IEEE. Copyright restrictions may apply. doi:10.1109/ITHERM.2018.8419483

$$\frac{L_e}{D_h} \approx 0.06\,\mathrm{Re}_{D_h} \text{ , for laminar flow } (\mathrm{Re}_{D_h} \le 2300) \quad (11)$$

$$\frac{L_e}{D_h} \approx 4.4\,\mathrm{Re}_{D_h}^{1/6} \text{, for turbulent flow } (\mathrm{Re}_{D_h} > 2300) \quad (12)$$

where, D_h is the channel hydraulic diameter and calculated as below

$$D_h = \frac{2bH}{b+H} \quad (13)$$

Re_{Dh} in the RHS of Eqs. (11) and (12) is the Reynolds number of the fluid flow based on the channel hydraulic diameter

$$\mathrm{Re}_{D_h} = \frac{U_{ch}.D_h}{\nu} \quad (14)$$

In order to calculate the channel flow velocity (U_{ch}),

$$U_{ch} = \frac{\dot{m}_{ch}}{\rho.H.b} \quad (15)$$

the channel mass-flow rate ($\dot{m}_{ch}$) should be calculated first

$$\dot{m}_{ch} = \frac{m_C}{N_f - 1} \quad (16)$$

and to calculate the channel mass flow rate the mass flow rate of the hot or cold stream through the one column of heat sinks or cold plates ($\dot{m}_C$) need to be calculated in prior.

$$\dot{m}_C = \frac{\dot{m}}{N_C} \quad (17)$$

where, $\dot{m}$ is the mass flow rate of the hot or cold fluid flowing through the duct attached to the bottom or the top side of the TEG array shelf. For the hot stream, $\dot{m}$ is calculated knowing the mass flow rate of the fuel cell exhaust gas and the number of server racks equipped with TEG modules shelf through the following equation

$$\dot{m} = \frac{\dot{m}_{exhaust}}{N_{TEG-Rack}} \quad (18)$$

For the cold stream, $\dot{m}$ is calculated knowing the volumetric flow rate of the cooling water in each server rack

$$\dot{m} = \rho.Q \quad (19)$$

Following the calculation of $\dot{m}$ and knowing the number of TEG columns, $\dot{m}_C$ is calculated through Eq. (17). According to Eq. (16), in addition to $\dot{m}_C$, the number of channels (N_f-1) should be also calculated in order to calculate $\dot{m}_{ch}$.

$$N_f = \left\lfloor \frac{W_{TEG} + b}{t + b} \right\rfloor \quad (20)$$

Through Eqs (11)-(20) the channel entrance length is calculated. Now, two scenarios might happen. The first scenario happens when the heat sink/cold plate length is less than or equal to the calculated entrance length ($L_{TEG} \le L_e$). It means that the flow throughout the channel remains in the hydraulic entrance or developing flow region. In this case the Nu correlation of Stephan [10], which was developed to calculate the overall Nusselt number for thermally and hydraulically developing flow, is used.

$$Nu = 7.55 + \frac{0.024 x_*^{-1.14}}{1 + 0.0358\,\mathrm{Pr}^{0.17} x_*^{-0.64}} \quad \text{for} \quad 0.1 \le \mathrm{Pr} \le 1000 \quad (21)$$

where x_* is the dimensionless distance from the inlet of the ducts attached to the TEG array shelf and calculated as below [10]

$$x_* = \frac{x / D_h}{\mathrm{Re}_{D_h}.\mathrm{Pr}} \quad (22)$$

In the equation above, x is the distance from the inlet of the ducts attached to the TEG array shelf.

In the second scenario, the hydraulic entrance length is less than the heat sink/cold plate length ($L_e < L_{TEG}$). It means that the flow through the channel reaches to hydraulically fully-developed region. Therefore, the Nu correlation of Teertstra et al. [11], which was developed based on a combination of fully developed and developing flow regimes in a parallel plate channel, should be applied.

for $0.1 \le \mathrm{Re}^*_b \le 100$ (23)

$$Nu = \left[\frac{1}{\left(\frac{\mathrm{Re}^*_b\,\mathrm{Pr}}{2}\right)^3} + \frac{1}{\left(0.664\sqrt{\mathrm{Re}^*_b}\,\mathrm{Pr}^{1/3}\sqrt{1 + \frac{3.65}{\sqrt{\mathrm{Re}^*_b}}}\right)^3} \right]^{-1/3}$$

where,

$$\mathrm{Re}^*_b = \frac{U_{ch} b}{\nu}\left(\frac{b}{L}\right) \quad (24)$$

Following the calculation of Nu number, the convection heat transfer coefficient is calculated.

$$h = \frac{Nu.k_{fluid}}{\lambda} \quad (25)$$

In the equation above, $\lambda = D_h$ in the case of first scenario when the Stephan's correlation is used to calculate Nu number. However, $\lambda = b$ in the case of second scenario when the Teertstra's correlation is used to calculate Nu number.

By the calculation of the convection heat transfer coefficient, the NTU is calculated as follows

This is an author-produced, peer-reviewed version of this article. The final, definitive version of this document can be found online at *Proceedings of the Seventeenth InterSociety Conference on Thermal and Thermomechanical Phenomena in Electronic Systems: Itherm 2018*, published by IEEE. Copyright restrictions may apply. doi: 10.1109/ITHERM.2018.8419483

$$NTU = \frac{h.A}{\dot{m}_{ch}.c_{Pfluid}} \quad (26)$$

As we see by the calculation of η_O from Eq. (5) and NTU from Eq. (24), the effectiveness (ε) is determined through Eq. (4) and subsequently the thermal resistance of heat sink or cold plate is calculated.

Calculation of hot and cold fluids thermal properties. In proceeding with the equations presented in the previous section, in calculating the heat sink/cold plate effectiveness, we also need to calculate thermal properties of the fuel cell exhaust gas and the server rack cooling water at different temperatures and pressures. To calculate water properties REFPROP subroutine program is used. This subroutine was developed by the National Institute of Standards and Technology (NIST) and more information in this regard can be found in [12]. However, the calculation of the fuel cell exhaust gas is more challenging as it is a mixture of two constituents including CO_2 and H_2O. Assuming the fuel cell exhaust gas is an ideal gas mixture, the thermal properties of the hot fluid in our system is calculated as below.

Density:

Recalling the following equation for the calculation of the molar specific volume of the ideal mixture [13]

$$\bar{\upsilon}_{Mix} = \sum_i y_i \bar{\upsilon}_i \quad (27)$$

Combining the above equation with the following equation

$$\bar{\upsilon} = \frac{M}{\rho} \quad (28)$$

The following equation for the calculation of the density of the mixture is derived.

$$\rho_{Mix} = \frac{M_{Mix}}{\sum_i \frac{y_i M_i}{\rho_i}} \quad (29)$$

where y_i is the molar fraction and calculated as below

$$y_i = \frac{n_i}{n_{Mix}} \quad (30)$$

Heat capacity:

The heat capacity of the ideal gas mixture is calculated through the following equation [13]

$$c_{p,Mix} = \sum_i mf_i c_{p,i} \quad (31)$$

where mf_i is the mass fraction and calculated as below

$$mf_i = \frac{m_i}{m_{Mix}} = y_i \frac{M_i}{M_{Mix}} \quad (32)$$

Dynamic viscosity:

The dynamic viscosity of the ideal gas mixture is calculated using the following equation [14]

$$\mu_{Mix} = \sum_i \frac{\mu_i}{1 + \frac{1}{y_i}\sum_{j \neq i} y_j \phi_{ij}} \quad (33)$$

where

$$\phi_{ij} = \frac{\left[1 + (\mu_i/\mu_j)^{\frac{1}{2}} (M_j/M_i)^{\frac{1}{4}}\right]^2}{(4/\sqrt{2})\left[1 + (M_i/M_j)\right]^{\frac{1}{2}}} \quad (34)$$

Thermal conductivity:

The thermal conductivity of the ideal gas mixture is calculated based on kinetic theory as [15]

$$k_{Mix} = \sum_i \frac{k_i}{1 + \sum_{j \neq i} \left(\frac{y_j}{y_i}\right)\left(\frac{M_{ij}}{M_i}\right)^{1/8} \phi_{ij}} \quad (35)$$

where ϕ_{ij} is calculated from Eq. (34) and $M_{ij} = (M_i + M_j)/2$.

It is required to mention that in calculation of the gas mixture thermal properties, using Eqs. (27)-(35), REFPROP is used to calculate the thermal properties of pure components. By the calculation of thermal properties, the Prandtl number (Pr) is calculated through the following equation.

$$\Pr = \frac{\mu . c_p}{k} \quad (36)$$

Considering the following cumulative form of reactions took place in the SOFC and knowing the molar mass of CO_2 and H_2O, the molar and mass fractions of the exhaust gas mixture components as well as the mixture molar mass are calculated which are presented in Table 2.

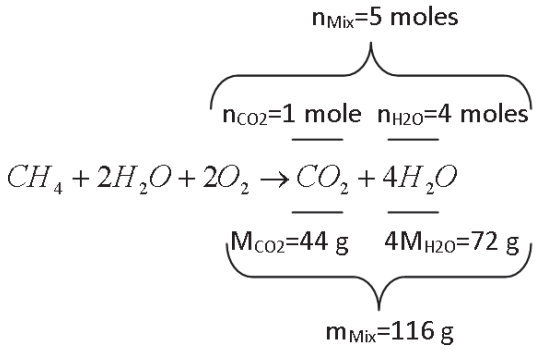

Fig. 7 Cumulative form of Reduction and Oxidation reactions took place separately in SOFC

Table 2. Molar and mass fractions of the fuel cell exhaust gas components as well as the molar mass of the gas mixture

Molar/Mass fraction	Value

This is an author-produced, peer-reviewed version of this article. The final, definitive version of this document can be found online at *Proceedings of the Seventeenth InterSociety Conference on Thermal and Thermomechanical Phenomena in Electronic Systems: Itherm 2018*, published by IEEE. Copyright restrictions may apply. doi: 10.1109/ITHERM.2018.8419483

CO_2	0.2, molar
CO_2	0.38, mass
H_2O	0.8, molar
H_2O	0.62, mass

The molar mass of the gas mixture is 23.2 g/mole

Optimization procedure. As mentioned earlier all heat sinks and cold plates have the same base area as that of TEG modules (1in x 1in). Therefore, the width and the length of heat sinks and cold plates are fixed dimensions. However, there are other dimensions in the heat sink and cold plate that can be changed and optimized to achieve the minimum possible thermal resistance formulated in Eq. (3). These dimensions are the fin thickness (t), fin height (H), base height (H_b) and fin spacing (b). Assuming that the fin thickness and base height are equal, the optimization parameters can be reduced to three. Considering baseline values for fin thickness and fin height, as presented in Table 3, the fin spacing is assigned as the only optimization parameter. After determining the optimum fin spacing, by fixing the fin spacing at its optimum value, the effects of fin height and fin thickness on the thermal resistance are investigated.

Design optimization calculations start with an initial guess for the optimization parameter which is the fin spacing. The initial guess can be made based on the information presented in Table 4 and the curve fit equations extracted from this Table which suggests optimal values for fin spacing based on flow velocity and fin length [16]. The flow velocity in Table 4 is calculated through the following equation

$$U = \frac{\dot{m}_C}{\rho . W_{TEG} . H} = \frac{Q_C}{W_{TEG} . H} \qquad (37)$$

Table 3. Fixed and baseline dimensions for heat sink and cold plate (see Fig.6)

Dimensions	Heat Sink	Cold Plate
Base width, W_{TEG} (FIXED)	25.4 mm	25.4 mm
Base length, L_{TEG} (FIXED)	25.4 mm	25.4 mm
Base height (BASELINE)	0.25 mm	0.8 mm
Fin thickness (BASELINE)	0.25 mm	0.8 mm
Fin height (BASELINE)	0.4 RU	0.3 RU

Table 4. Guidelines for selecting fin spacing based on flow velocity and fin length [16]

Dimensions	L_f=75 mm	L_f=150 mm	L_f=225 mm	L_f=300 mm
Natural Convection	b=6.5 mm	b=7.5 mm	b=10 mm	b=13 mm
1.0	b=4 mm	b=5 mm	b=6 mm	b=7 mm
2.5	b=2.5 mm	b=3.3 mm	b=5 mm	b=7.5 mm
5.0	b=2 mm	b=2.5 mm	b=3 mm	b=3.5 mm

Thermoelectric Calculations and Optimization

According to the algorithm presented in Fig. 5, the thermoelectric calculations and optimization start with an initial guess for TE element thickness (d). The TE element thickness is updated in every loop of calculations until the maximum TEG power output is achieved. To proceed with the procedure of calculations within in the loop shown in Fig. 5, the temperatures of the hot and cold sides of the TE element (T_h and Tc, respectively) should be calculated as well. In order to calculate T_h and T_c, the TEG internal and external thermal resistances need to be calculated. In this section, first the formulations for the calculation of thermal resistances are presented. Then, the recursive algorithm through which T_h and T_c are calculated is introduced. By the calculation of the hot and cold side temperatures of TE element, the procedure of calculations to find the optimum thickness for the TE element is explained. Finally, the formulations for the calculation of electrical resistances and the TEG power output are explained.

Calculation of the TEG external and internal thermal resistances. As shown in Figs 8 and 9, the external thermal resistances are created by the convection thermal resistance between the heating/cooling fluid flow and the heat sink/cold plate, conduction thermal resistance in Heat sink/cold plate, conduction thermal resistance in TIMs, as well as conduction and contraction thermal resistances in the TEG substrates. The equations used for the calculation of the mentioned thermal resistances are presented in Table 5.

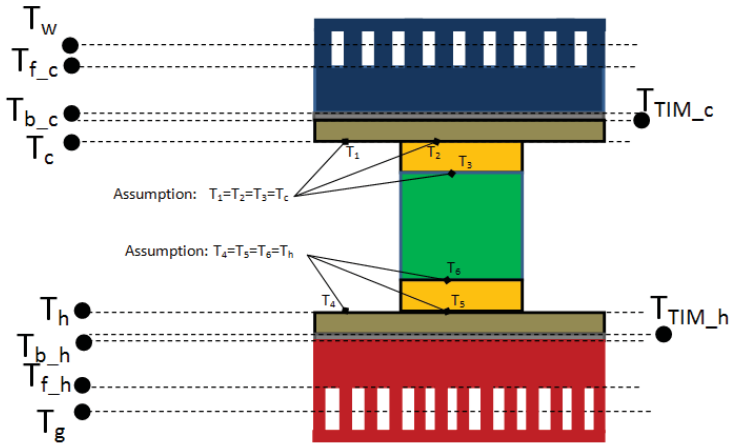

Fig. 8 A cross-section of TEG module with one leg and the attached heat sink and cold plate

This is an author-produced, peer-reviewed version of this article. The final, definitive version of this document can be found online at *Proceedings of the Seventeenth InterSociety Conference on Thermal and Thermomechanical Phenomena in Electronic Systems: Itherm 2018*, published by IEEE. Copyright restrictions may apply. doi: 10.1109/ITHERM.2018.8419483

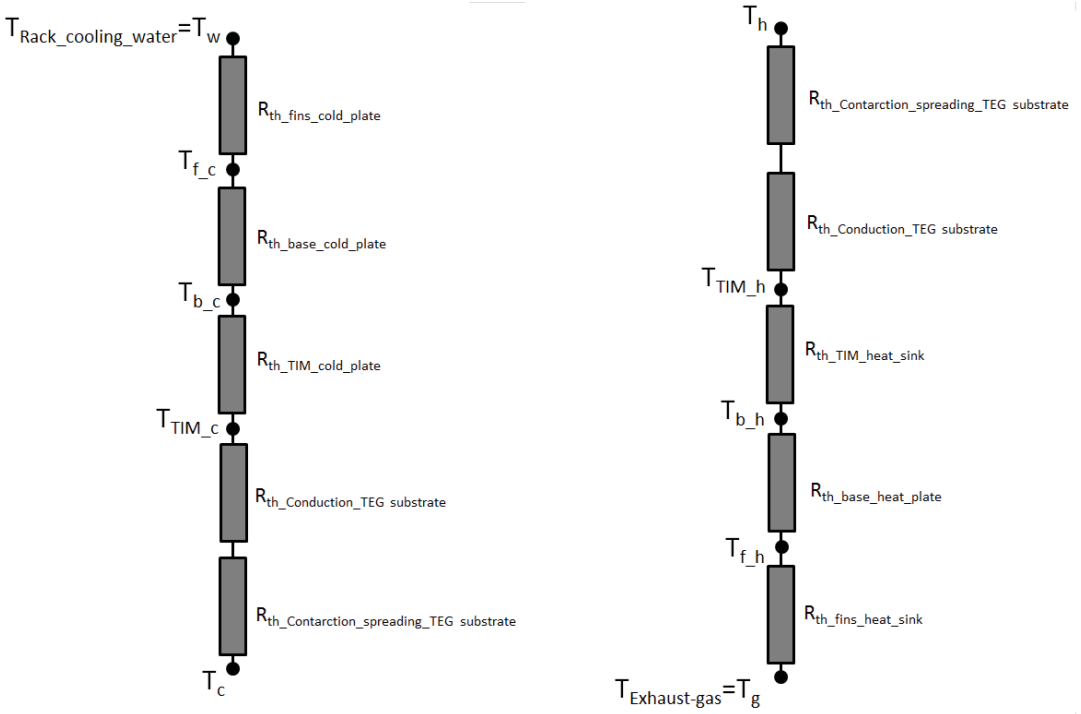

Fig. 9 Arrangement of external thermal resistances on cold and hot sides of TEG module

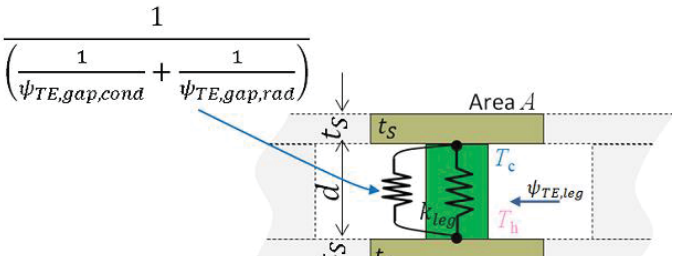

Fig. 10 Components of TEG internal thermal resistances

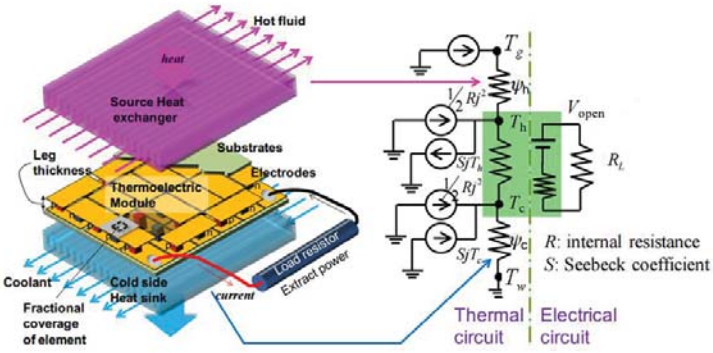

Fig. 12 TEG module and the electro-thermal coupling within TE element [5,6]

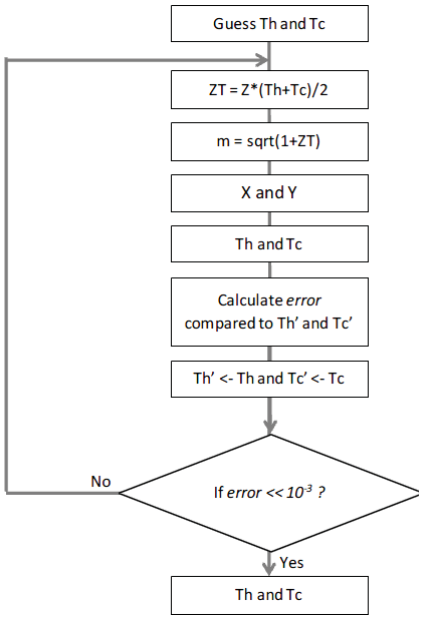

Fig. 11 Recursive algorithm to calculate TE element hot and cold side temperatures [5,6]

This is an author-produced, peer-reviewed version of this article. The final, definitive version of this document can be found online at *Proceedings of the Seventeenth InterSociety Conference on Thermal and Thermomechanical Phenomena in Electronic Systems: Itherm 2018*, published by IEEE. Copyright restrictions may apply. doi: 10.1109/ITHERM.2018.8419483

Table 5. External thermal resistances and the corresponding equations

Components of the External Thermal Resistance (K/W)	Corresponding Equation- Hot Side	Corresponding Equation- Cold Side
Heat Sink fins	$R_{th-HS\_fins} = \frac{1}{\dot{m}_c c_{p_g} \varepsilon_{HS}}$ (38)	NA
Heat Sink base	$R_{th-HS\_base} = \frac{H_b}{k_{HS}.A_b}$ (39)	NA
Cold plate fins	NA	$R_{th-CP\_fins} = \frac{1}{\dot{m}_{c,w} c_{pw} \varepsilon_{CP}}$ (40)
Cold plate base	NA	$R_{th-CP\_base} = \frac{H_{bCP}}{k_{CP}.A_b}$ (41)
TIM	$R_{th-TIM} = \frac{t_{TIM}}{k_{TIM}.A_b}$ (42)	$R_{th-TIM} = \frac{t_{TIM}}{k_{TIM}.A_b}$ (42)
Substrate conduction	$R_{th-sub-cond} = \frac{t_s}{k_s.A_b}$ (43)	$R_{th-sub-cond} = \frac{t_s}{k_s.A_b}$ (43)
Substrate contraction [17]	$R_{th-sub-cont} = \frac{(1-\sqrt{F})^{3/2}}{2k_s\sqrt{FA_b}} \frac{\tanh(\lambda_c\tau) + \frac{\lambda_c}{Bi_h}}{1+\frac{\lambda_c}{Bi_h}\tanh(\lambda_c\tau)}$ (44) $\tau = \frac{t_s}{\sqrt{\frac{A_b}{\pi}}}$ (46), $Bi_h = \frac{1}{k_s.R_h\sqrt{\pi A_b}}$ (47) $R_h = R_{th-HS\_fins} + R_{th-HS\_base} + R_{th-TIM}$ (49) $\lambda_c = \pi + \frac{1}{\sqrt{\pi F}}$ (51)	$R_{th-sub-cont} = \frac{(1-\sqrt{F})^{3/2}}{2k_s\sqrt{FA_b}} \frac{\tanh(\lambda_c\tau) + \frac{\lambda_c}{Bi_c}}{1+\frac{\lambda_c}{Bi_c}\tanh(\lambda_c\tau)}$ (45) $\tau = \frac{t_s}{\sqrt{\frac{A_b}{\pi}}}$ (46), $Bi_c = \frac{1}{k_s.R_c\sqrt{\pi A_b}}$ (48) $R_c = R_{th-CP\_fins} + R_{th-CP\_base} + R_{th-TIM}$ (50) $\lambda_c = \pi + \frac{1}{\sqrt{\pi F}}$ (51)
Resultant (Km^2/W)	$\psi_h = R_{th-HS\_fins}.A + (R_{th-HS\_base} + R_{th-TIM} + R_{th-sub-cond} + R_{th-sub-cont}).A_b$ (52)	$\psi_c = R_{th-CP\_fins}.A + (R_{th-CP\_base} + R_{th-TIM} + R_{th-sub-cond} + R_{th-sub-cont}).A_b$ (53)

This is an author-produced, peer-reviewed version of this article. The final, definitive version of this document can be found online at *Proceedings of the Seventeenth InterSociety Conference on Thermal and Thermomechanical Phenomena in Electronic Systems: Itherm 2018*, published by IEEE. Copyright restrictions may apply. doi: 10.1109/ITHERM.2018.8419483

Table 6. Internal thermal resistances and the corresponding equations

Components of the Internal Thermal Resistance (Km^2/W)	Corresponding Equation
TE leg conduction	$\psi_{TE,leg} = \frac{d}{k_{leg}.F}$ (54)
TE gap conduction	$\psi_{TE,gap,cond} = \frac{d}{k_{leg}.(1-F)}$ (55)
TE gap radiation	$\psi_{TE,gap,rad} = \frac{d}{\varepsilon\sigma_{SB}(1-F)(T_h^2+T_c^2)(T_h+T_c)}$ (56) ε the substrate emissivity
	$\sigma_{SB} = 5.670367(13)\times10^{-8}$ W m^{-2} K^{-4}
Resultant	$\psi_0 = \frac{1}{\frac{1}{\psi_{TE,leg}}+\frac{1}{\psi_{TE,gap,cond}}+\frac{1}{\psi_{TE,gap,rad}}}$ (57)

Figure 11 shows that the internal thermal resistance (ψ_0) is the resultant of three parallel thermal resistances including conduction thermal resistance in TE element ($\psi_{TE,leg}$) as well as conduction and radiation thermal resistances in the gap between the TEG substrates ($\psi_{TE,gap,cond}$ and $\psi_{TE,gap,rad}$) [5,6].

Recursive algorithm for the calculation of T_h and T_c. In order to start the calculations within the recursive algorithm, as shown in Fig. 11, initial guesses for T_h and T_c are made based on the maximum TEG power output for symmetric thermal resistances in the hot and cold sides of a TEG module with $Z << 1$ [5].

$$T_h = \frac{1}{4}(3T_g + T_w)$$
$$T_c = \frac{1}{4}(T_g + 3T_w) \quad (58)$$

According to thermal and electrical impedance matching, the electrical resistance ratio in TE element (m) is calculated as below [5] (see Fig. 12)

$$m = \sqrt{1+Z\bar{T}} \quad (59)$$

where Z is the figure of merit of TE material and $\bar{T}$ is the average temperature between the TE hot and cold sides:

$$Z = \sigma S^2 / k_{leg} \quad (60)$$

$$\bar{T} = \frac{T_h + T_c}{2} \quad (61)$$

As elaborately explained in Ref. [5], by solving the governing energy balance equations for the thermal circuit in TEG module (see Fig. 12) the relation of the temperature differences becomes

$$\frac{T_h - T_c}{T_g - T_w} = \frac{d}{d + k_{leg}F(X+Y)} \quad (62)$$

where,

$$X = \left(1 + \frac{Z}{2(1+m)^2}((2m+1)T_h + T_c)\right)\psi_h \quad (63)$$

$$Y = \left(1 + \frac{Z}{2(1+m)^2}(T_h + (2m+1)T_c)\right)\psi_c \quad (64)$$

ψ_h and ψ_c are the hot and cold side external thermal resistances per unit heat transfer surface area and calculated through Eqs. (52) and (53).

To find new values for T_h and T_c, the governing energy balance equations are solved such that T_h and T_c are found in terms of X, Y, ψ_0 and temperatures of the hot and cold fluids (T_g and T_w)[5]:

$$T_h = \frac{1}{(X+Y)+\psi_0}\left((Y+\psi_0)T_g + XT_w\right) \quad (65)$$

$$T_c = \frac{1}{(X+Y)+\psi_0}\left(YT_g + (X+\psi_0)T_w\right) \quad (66)$$

X, Y, ψ_0 in the RHS of Eqs. (65) and (66) are calculated through Eqs. (63), (64), and (57), respectively, using the initial guesses for T_h and T_c from Eq. (58). The new T_h and T_c are then used to repeat the calculations in the recursive algorithm and the loop of calculations continues until converged values for T_h and T_c are achieved (with the maximum relative deviation of 10^{-3}).

Optimization of TE element (leg) thickness. After the calculation of T_h and T_c, the loop of calculations in the algorithm depicted in Fig. 5 is completed. By the calculation of a new value for the TE element (leg) thickness at the end of each loop and considering that as the new input for the next loop, the loop of calculations is repeated until a converged value for *d* is achieved (with the maximum relative deviation of 10^{-3}). The new value for *d* is calculated using the following equation, derived by Yazawa and Shakouri [5], for the optimum TE element thickness.

$$d_{opt} = \kappa.k_{leg}.F.\sum\psi \quad (67)$$

where $\sum\psi = \psi_h + \psi_c$ and κ is a dimensionless factor which is calculated as below

$$\kappa = \frac{1}{\sum\Psi}(X\Psi_h + Y\Psi_c) \quad (68)$$

This is an author-produced, peer-reviewed version of this article. The final, definitive version of this document can be found online at *Proceedings of the Seventeenth InterSociety Conference on Thermal and Thermomechanical Phenomena in Electronic Systems: Itherm 2018*, published by IEEE. Copyright restrictions may apply. doi: 10.1109/ITHERM.2018.8419483

In the equation above,

$$\Psi_h = R_{th-HS\_fins} + R_{th-HS\_base} + R_{th-TIM} + R_{th-sub-cond} + R_{th-sub-cont} \quad (69)$$

$$\Psi_c = R_{th-CP\_fins} + R_{th-CP\_base} + R_{th-TIM} + R_{th-sub-cond} + R_{th-sub-cont} \quad (70)$$

$$\sum \Psi = \Psi_h + \Psi_c \quad (71)$$

Electrical resistances and power calculations. Considering N as the number of TE legs per unit area of the TEG module, the internal resistance of each TE element (leg) is calculated as below

$$R_0 = \frac{d}{\sigma F A_b} = N \frac{d}{\sigma F} \quad (72)$$

The module internal resistance of *N* legs in series per unit area of the TEG module is then calculated through the following equation.

$$R_{\text{int}} = NR_0 = N^2 \frac{d}{\sigma F} \quad (73)$$

Knowing the electrical resistance ratio, *m* from Eq. (59), the external resistance is calculated.

$$R_{ext} = mR_{\text{int}} \quad (74)$$

The load resistance (R_L) is found to match to the maximum power output,

$$R_L = R_{ext} - 2NR_{ec} + (2N-1)R_{es} \quad (75)$$

where R_{ec} is the contact electrical resistance and R_{es} is the series resistance between the contacts. R_{ec} and R_{es} are calculated as below:

$$R_{ec} = \frac{\rho_{ec}}{FA_b} \quad (76)$$

where ρ_{ec} is the specific contact resistivity and,

$$R_{es} = \frac{1-F}{\sigma_{el} d_{el}} \quad (77)$$

More precise analysis considering the electrical current flow contraction at the contact was reported in Ref. [18]. The difference in practical application is small.

As we have N series of open circuit voltage per unit area of TEG module, the electric current can be calculated as below:

$$I = \frac{NV}{R_{ext} + R_{\text{int}}} = \frac{NV}{(1+m)R_{\text{int}}} \quad (78)$$

where V is the induced open circuit electric potential for each TE element which is calculated through the following equation.

$$V = S(T_h - T_c) \quad (79)$$

where S is the Seebeck coefficient.

Finally, knowing the load resistance and the electric current, the power output per unit area of the TEG module is calculated as below:

$$w = I^2 R_L \quad (80)$$

Procedure of calculations for one column of TEG array. The calculations are performed for a column of TEG modules as shown in Fig. 3. The number of TEG modules in the column is equal to the number of TEG array rows as shown in Fig. 3 and calculated through Eq. (1). As mentioned earlier same heat sinks and same cold plates are attached to hot and cold substrates of the TEG modules. Design optimization for both heat sink and cold plate is performed based on the flow conditions at the inlet of the column. Knowing the temperature of fluid at the inlet of heat sink/cold plate, the temperature at the outlet of the heat sink/cold plate is calculated through the calculation of the heat sink/cold plate fin temperature and implementation of effectiveness for the constant surface temperature heat sink/cold plate.

Heat Sink	Cold Plate
$q_{h,i} = \frac{T_{g,i} - T_{h,i}}{\psi_{h,i}} = \frac{T_{g,i} - T_{f\_h,i}}{R_{th-HS\_fins,i}}$ (81)	$q_{c,i} = \frac{T_{c,i} - T_{w,i}}{\psi_{c,i}} = \frac{T_{f\_c,i} - T_{w,i}}{R_{th-CP\_fins,i}}$ (82)
$\varepsilon_{HS,i} = \frac{T_{g,i+1} - T_{g,i}}{T_{f\_h,i} - T_{g,i}}$ (83)	$\varepsilon_{CP,i} = \frac{T_{w,i+1} - T_{w,i}}{T_{c\_h,i} - T_{w,i}}$ (84)

The power generated by one column of TEG modules, the amount of heat extracted from the exhaust gas by one column of heat sinks and the heat released to cooling water by one column of cold plate are calculated by Eqs. (85) -(87), respectively.

$$W_C = \sum_{i=1}^{i=N_R} w_i A_b \quad (85)$$

$$Q_{h,C} = \sum_{i=1}^{i=N_R} \frac{(T_{g,i} - T_{h,i})}{\psi_{h,i}} A_b \quad (86)$$

$$Q_{c,C} = \sum_{i=1}^{i=N_R} \frac{(T_{c,i} - T_{w,i})}{\psi_{c,i}} A_b \quad (87)$$

The efficiency of the one column of TEG modules is calculated as below:

$$\eta = \frac{W_C}{Q_{h.C}} \quad (88)$$

The friction pressure drop of the hot and cold fluid flows along the column of the heat sinks and cold plates are calculated using the following equations.

$$\Delta P = f \frac{x}{D_h} (\rho \frac{U_{ch}^{\ 2}}{2}) \quad (89)$$

where *f* is the friction factor and

This is an author-produced, peer-reviewed version of this article. The final, definitive version of this document can be found online at *Proceedings of the Seventeenth InterSociety Conference on Thermal and Thermomechanical Phenomena in Electronic Systems: Itherm 2018*, published by IEEE. Copyright restrictions may apply. doi: 10.1109/ITHERM.2018.8419483

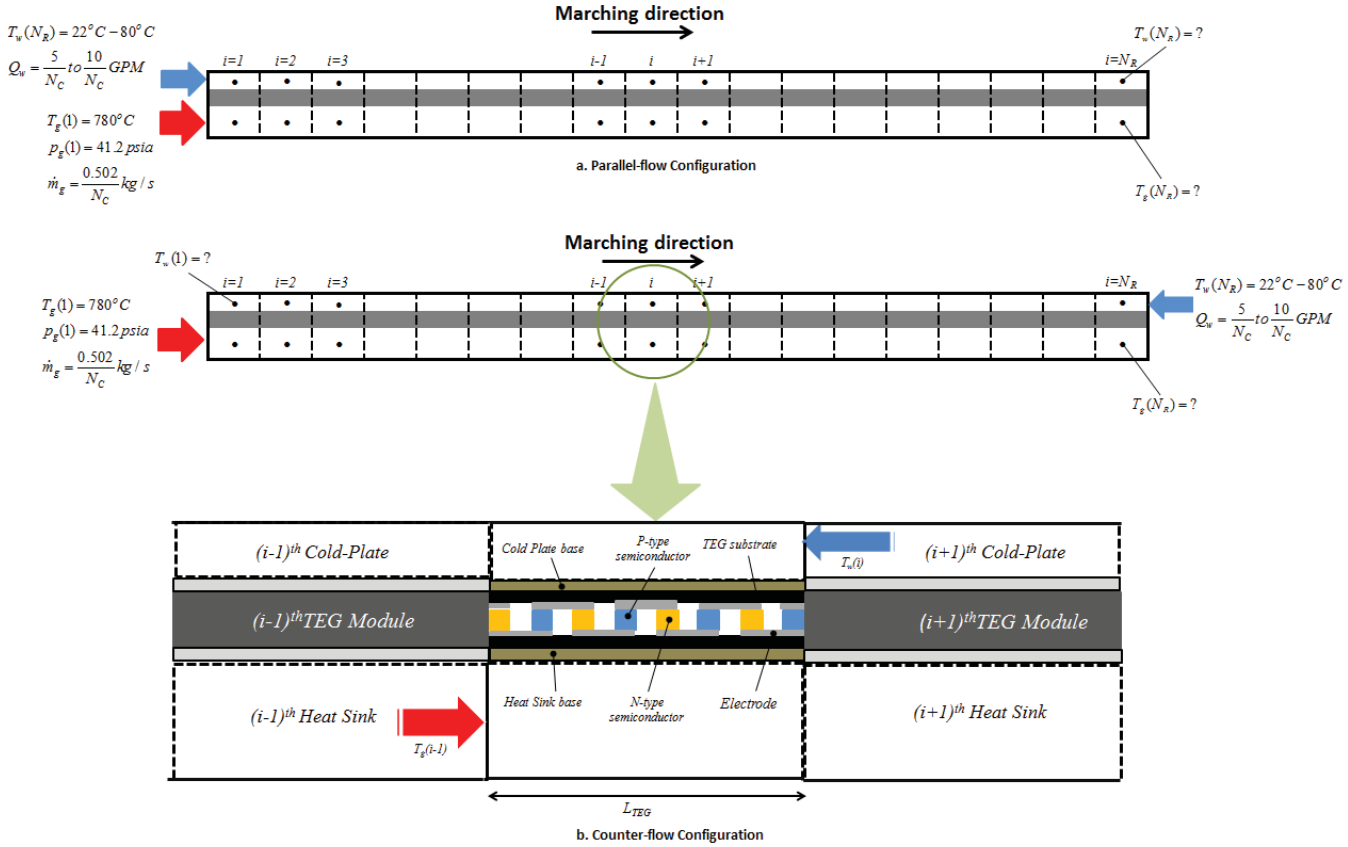

Fig. 13 Schematic view of one column of thermo-electric heat exchanger

$$f = f_{FD} = \frac{1}{\mathrm{Re}_{D_h}}\left[19.64\left(\frac{\left(\frac{b}{H}\right)^2+1}{\left(\frac{b}{H}+1\right)^2}\right)+4.7\right], \quad \text{for fully developed flow [19]} \tag{90}$$

$$f = f_{app} = \frac{1}{\mathrm{Re}_{D_h}}\left\{\left[3.2(x^+)^{-0.57}\right]^2+(f_{FD}\,\mathrm{Re}_{D_h})^2\right\}^{1/2}, \quad \text{for developing flow [20]} \tag{91}$$

x^+ in the equation above is the dimensionless distance from the channel inlet and defined as below:

$$x^+ = \frac{x}{\mathrm{Re}_{D_h}} \tag{92}$$

Fig. 13 Schematic view of one column of thermo-electric heat exchanger

Summary and Conclusion

Heat sink and cold plate design optimization and calculations

Design optimization was performed using the baseline values indicated in Table 3. Considering $\beta = 2/(b+t)$ as the optimization parameter, where b is the fin spacing and t is the fin thickness, Figs. 14 and 15 show the effect of fin spacing on the heat sink and cold plate thermal resistance and effectiveness. Three materials, with different thermal conductivities and softening temperatures, were considered as the heat sink material. They include Copper, Aluminum, and Iridium. Figure 14 indicates while materials with higher thermal conductivity seemed to be better choices in order to have higher effectiveness, the softening temperature also matters as the heat sink material should withstand the high temperature gas flow (700-800°C) and not deform. Among the three tested materials, Iridium has the highest softening temperature. For all tested materials, as $\beta \to 1750$, the thermal resistance reached to its minimum values of ~0.34 for Copper, ~0.39 for Aluminum and ~0.42 for Iridium . If Iridium is selected as the heat sink material, then the optimum fin spacing will be ~0.9 mm. In this case, effectiveness reaches to its maximum possible value of 0.7 as $b \to 0.9mm$. For the fin spacing less than 0.9 mm, the Reynolds number decreases and resulted in decreasing Nusselt

This is an author-produced, peer-reviewed version of this article. The final, definitive version of this document can be found online at *Proceedings of the Seventeenth InterSociety Conference on Thermal and Thermomechanical Phenomena in Electronic Systems: Itherm 2018*, published by IEEE. Copyright restrictions may apply. doi: 10.1109/ITHERM.2018.8419483

number or heat transfer coefficient increasing and subsequently increasing the thermal resistance. The heat sink calculations, presented in Fig. 14, were performed based on the exhaust gas thermal conditions indicated in Fig. 4.

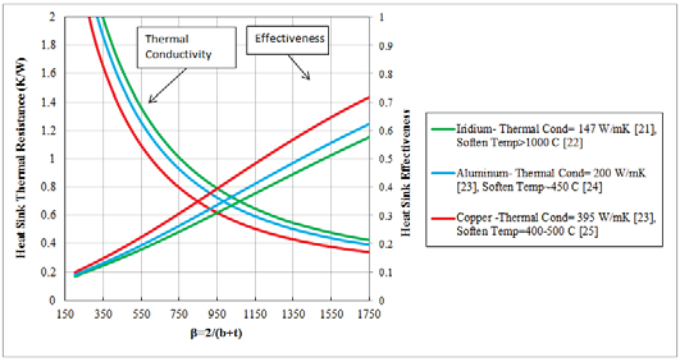

Fig. 14 Design optimization for the heat sink based on the fixed and baseline dimensions presented in Table 3.

Figure 15 shows the effect of fin spacing on the thermal resistance and effectiveness of the cold plate. Copper was selected as the cold plate material as it is among the common materials used in electronics packaging which have highest thermal conductivities [23]. The design parameter, $\beta=2/(b+t_{CP})$, is defined based on the fin spacing. The thermal conditions of water at the inlet of cold plate are T=70°C, p=110 kPa and $\dot{m}_C$ =19.2 g/s. The optimization was performed based on the fixed and baseline values presented in Table 3. Figure 15 shows as $\beta \to 1400$ the cold plate thermal resistance achieves its minimum value of ~0.05. Selecting fin spacing of 1.1mm, a thermal resistance of 0.07 was achieved for the cold plate.

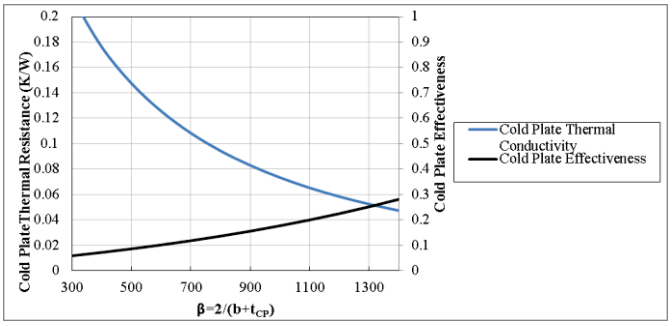

Fig. 15 Design optimization for the cold plate based on the fixed and baseline dimensions presented in Table 3.

Thermo-electric design optimization and calculations

Starting from counter-flow configuration, Fig. 16 shows the results for temperatures of the exhaust gas and cooling water as well as the hot and cold sides of the TE legs along one column of TEG arrays. The data presented in Table 1 were used as the base values for the TEG characteristics in the corresponding calculations shown in Fig. 16. The temperature difference between the exhaust gas and TE leg hot side is ~ 650 °C while the temperature difference between the cooling water and TE leg cold side is ~ 60 °C. This indicates the necessity of furthermore improving of heat transfer rate through decreasing of thermal resistance in the hot side. As explained in 3.1, due to space limitations, thermal resistance reduction cannot be accomplished through increasing the number of fins. Selecting materials with higher conductivity for heat sinks, TIM and substrate can be effective. Also increasing the mass-flow rate of exhaust gas can decrease the thermal resistance between the exhaust gas and TE hot side.

Fig 17 and 18 show the performance of TEG modules under the explained thermal conditions, heat sinks and cold plates design and TEG modules characteristics. In order to improve the efficiency of the system, the effect of the following parameters on the efficiency of the system are studied and discussed:

- Heat sink conductivity
- TIM thermal resistance
- Substrate thermal resistance
- TEG figure of merit, ZT
- TE leg thickness
- TEG Filling factor
- Exhaust gas mass flow rate and temperature
- Cooling water mass flow rate and temperature

Parametric study on the effect of heat sink conductivity on TEG module efficiency

The issue with heat sink material is it should have high thermal conductivity and softening temperature at the same time in order to achieve the reliably better performance of the system. Figure 19 shows the effect of thermal conductivity of the heat sink on the efficiency of TEG modules along one column of TEG arrays. Assuming that Aluminum and Copper can withstand the high temperature of the fuel cell exhaust gas, we see from Fig. 19 that by ~168% increase in thermal conductivity from 147 to 395 W/m/K, the TEG modules efficiency is improved by a maximum value of 6%. It shows the weak sensitivity of the system to heat sink thermal conductivity.

Parametric study on the effect of the TIM thermal resistance on TEG module efficiency

The thermal resistance can be decreased through decreasing the TIM thickness and/or using materials with higher thermal conductivity. The minimum thickness reported [16] is 0.002 in which is already considered as TIM thickness baseline value. However, the material can be changed from the baseline High Performance Thermal Compound with thermal conductivity of 0.03 W/in/C to A-Phi 220 with thermal conductivity of 0.074 W/in/C. A-Phi 220 is the TIM material with highest thermal conductivity reported by [16]. Figure 20 shows the effect of TIM thermal conductivity on the efficiency of TEG modules. As can be seen, by ~ 147% increase in TIM thermal conductivity, the efficiency increased by 4-7% which indicated the system performance sensitivity to TIM thermal conductivity is almost equivalent to its sensitivity to the heat sink thermal conductivity.

This is an author-produced, peer-reviewed version of this article. The final, definitive version of this document can be found online at *Proceedings of the Seventeenth InterSociety Conference on Thermal and Thermomechanical Phenomena in Electronic Systems: Itherm 2018*, published by IEEE. Copyright restrictions may apply. doi: 10.1109/ITHERM.2018.8419483

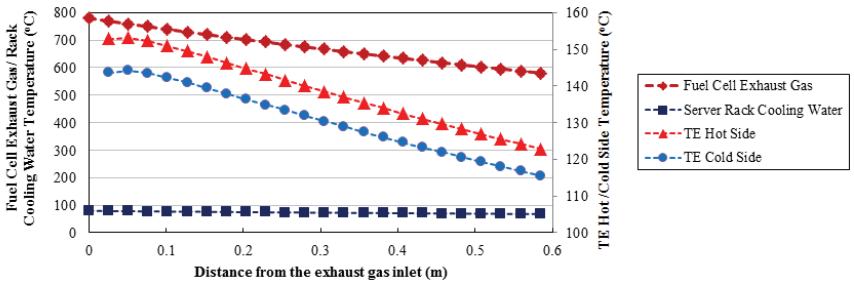

Fig. 16 Fuel cell exhaust gas and cooling water temperature along one column of TEG moguls (left vertical axis), as well as the temperatures of the TE leg hot and cold sides (right vertical axis).

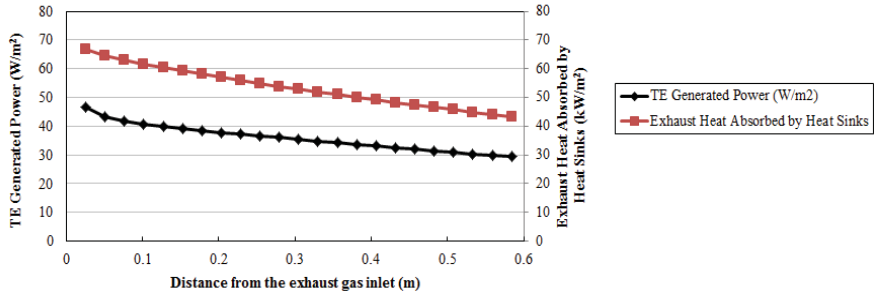

Fig. 17 TEG modules generated power (left vertical axis) and exhaust heat absorbed by heat sinks (right vertical axis) along one column of TEG moguls.

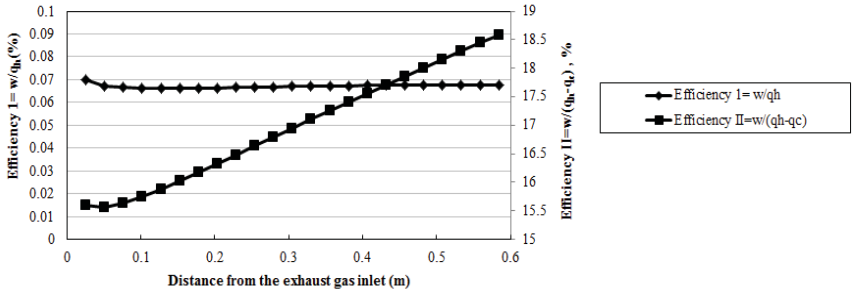

Fig. 18 TEG modules efficiency defined as either the ratio of the TE power to heat absorbed at heat sinks (left axis) or the ratio of the TE power to the heat absorbed by the TEG modules (right axis).

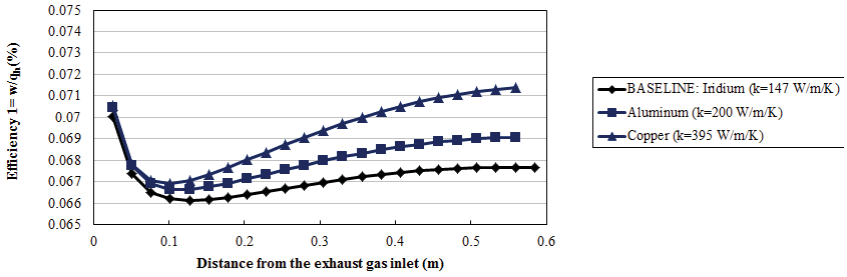

Fig. 19 Effect of thermal conductivity of the heat sink on the efficiency of TEG modules along one column of TEG arrays

This is an author-produced, peer-reviewed version of this article. The final, definitive version of this document can be found online at *Proceedings of the Seventeenth InterSociety Conference on Thermal and Thermomechanical Phenomena in Electronic Systems: Itherm 2018*, published by IEEE. Copyright restrictions may apply. doi: 10.1109/ITHERM.2018.8419483

Parametric study on the effect of the substrate thermal resistance on TEG module efficiency

The baseline TE calculations were performed assuming the substrate material is Al_2O_3 with thermal conductivity of 20 W/m/K and thickness of 1 mm. Boron Nitride (BN) with thermal conductivity of 600 W/m/k is the ceramic with highest thermal conductivity reported in [26]. Considering BN as the substrate ceramic, the effect of substrate thermal resistance on TEG modules efficiency is studied.

Fig 21 shows effect of substrate material on the efficiency of the TEG modules. Replacing the baseline material for substrate with another ceramic with 30-time higher thermal conductivity can result in up to 30% improvement in TEG modules efficiency as can be seen in Fig. 21.

Parametric study on the effect of TE Seebeck coefficient on TEG module efficiency

Figure 22 shows by increasing the TE element Seebeck coefficient from baseline value of $2.4x10^{-4}$ V/K to $2.6x10^{-4}$ V/K (~8% increase) the figure of merit of TEG moguls (ZT) by ~12% and the TEG modules efficiency is increased by ~7%.

Parametric study on the effect of TE leg thickness on TEG module efficiency

Figure 23 shows the strong effect of TE leg thickness on the efficiency of the TEG modules. By increasing the TE leg thickness, the efficiency of the system also increases. Any percent increase in the TE leg thickness will lead a ~ 0.7% increase in the TEG modules efficiency. By increasing the TE leg, the TE internal resistance also increases which makes the temperature difference between TE hot and cold sides become larger. By increasing the temperature difference, higher voltages are created by TE leg. Although by increasing the TE leg, the TE electrical load resistance also increases, the results shown in Fig. 23 indicate that the stronger sensitivity of TE created voltage to TE leg thickness has the dominant effect in increasing the TEG modules efficiency.

Parametric study on the effect of filling factor (F) on TEG module efficiency

Figure 24 shows the effect of filling factor on the efficiency of TEG modules. By increasing the filling factor from baseline value of 0.3 to 0.6 (100% increase), the experiences a 200% increase. Further increases in the filling factor from 0.6 to 0.9 (50% increase) leads to a ~ 150% increase in the efficiency. Finally, 10% increase in filling factor from 0.9 to 0.99 improves the efficiency by 17%. The parametric study on filling factor shows that the filling factor has the strongest effect on system efficiency compared to the other studied TE characteristics.

Parametric study on the effect of fuel cell exhaust gas mass flow rate on TEG module efficiency

In the baseline calculations, it was assumed that the exhaust gas mass flow rate of 0.502 kg/s is divided evenly between ~ 15 racks powered by the 220 kW SOFC. By decreasing the number of racks and consequently increasing the mass flow rate of the exhaust gas for each column of TEG modules, the efficiency of TEG modules increases especially at the end of the column (by ~16%).

Parametric study on the effect of cooling water mass flow rate on TEG module efficiency

As shown in Fig. 26, increasing the mass flow rate of cooling water from 5 GPM to maximum possible of 10 GPM does not have considerable effect on the TEG modules efficiency in average.

Introduction of an optimal case and performance analysis

Based on the analysis performed in section 3.2, an optimal TEG module with the following specifications is considered. The rest of characteristics are the same as those presented in Table 1.

Figure 27 shows the efficiency of the TEG modules under the conditions presented in Table 8 when filling factor (F) can change from 0.6 to 0.99. The corresponding ZT values are also shown in Fig. 28. Fig. 29 indicated the total power generated by one TEG shelf. Considering that four racks equipped with TEG shelf recover the waste heat dissipated by the 220 kW SOFC exhaust gas the total power output generated by TEG shelves could be as high as 5kW.

Figure 30 shows the superiority of counter-flow configuration compared to parallel flow in delivering higher energy conversion and waste heat recovery efficiencies.

Table 8. Optimal /examined parameters in optimal TE calculations

Parameter	Optimal/Examined values
Number of server racks equipped with a shelf of TEG modules	4
TEG module filling factor, F	0.6, 0.8.0.9, and 0.99
TE leg thickness, d	50×10^{-4}m
Seebeck coefficient, S	2.6×10^{-4}V/K
Substrate (BN) conductivity, k_s	600 W/m/K
TIM thermal conductivity, k_{TIM}	2.92 W/m/K
Heat sink thermal conductivity, k_{HS}	147/W/m/K
Cooling water inlet temperature, $T_{c\text{-}i}$	15^{o}C

This is an author-produced, peer-reviewed version of this article. The final, definitive version of this document can be found online at *Proceedings of the Seventeenth InterSociety Conference on Thermal and Thermomechanical Phenomena in Electronic Systems: Itherm 2018*, published by IEEE. Copyright restrictions may apply. doi: 10.1109/ITHERM.2018.8419483

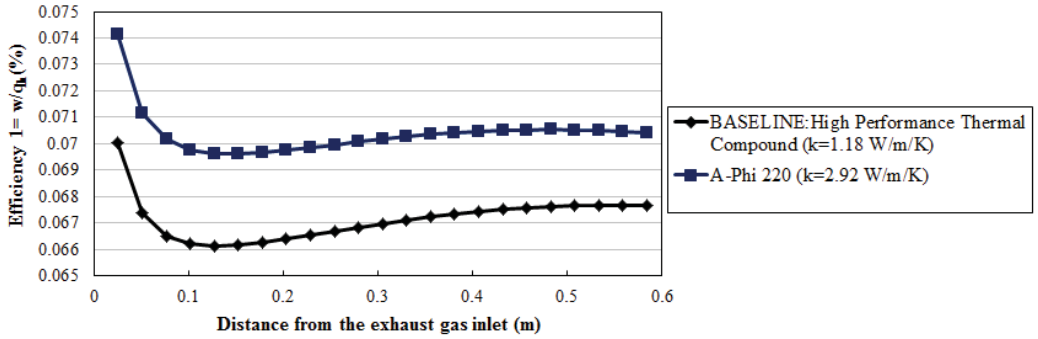

Fig. 20 Effect of thermal conductivity of the TIM on the efficiency of TEG modules along one column of TEG arrays

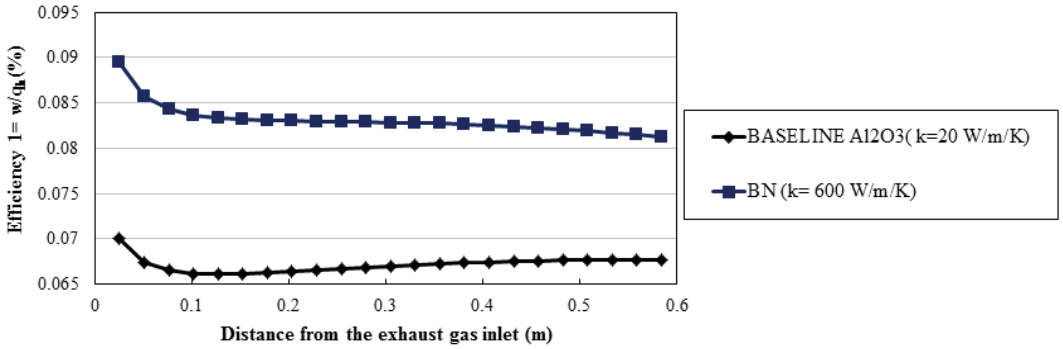

Fig. 21 Effect of thermal conductivity of the substrate ceramic on the efficiency of TEG modules along one column of TEG arrays

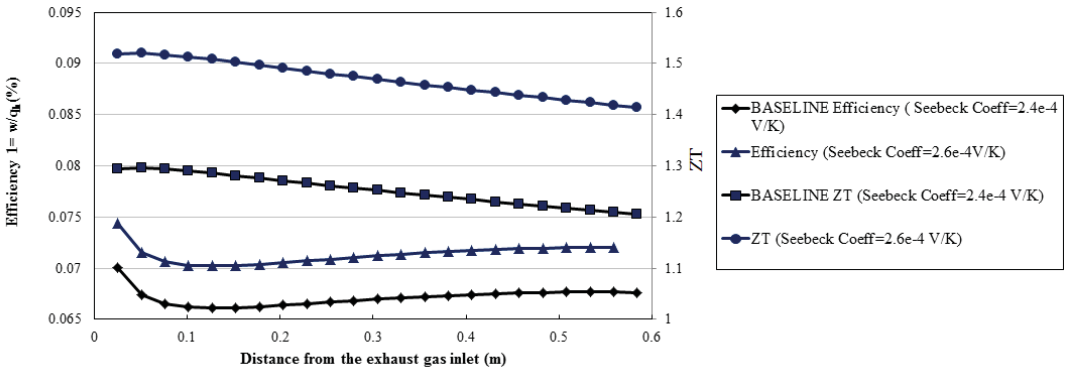

Fig. 22 Effect of TE Seebeck coefficient on the efficiency of TEG modules along one column of TEG arrays

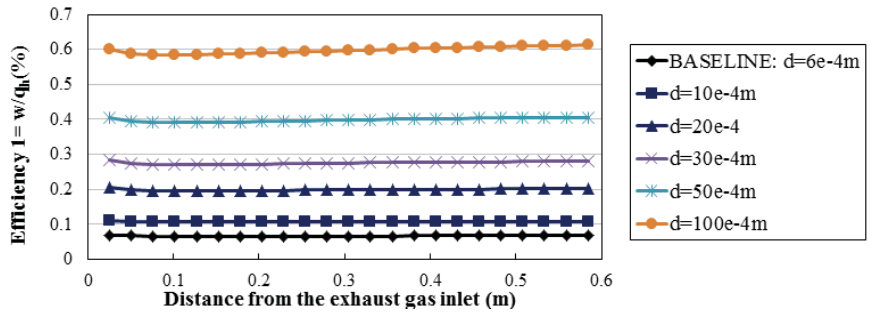

Fig. 23 Effect of TE leg thickness on the efficiency of TEG modules along one column of TEG arrays

This is an author-produced, peer-reviewed version of this article. The final, definitive version of this document can be found online at *Proceedings of the Seventeenth InterSociety Conference on Thermal and Thermomechanical Phenomena in Electronic Systems: Itherm 2018*, published by IEEE. Copyright restrictions may apply. doi: 10.1109/ITHERM.2018.8419483

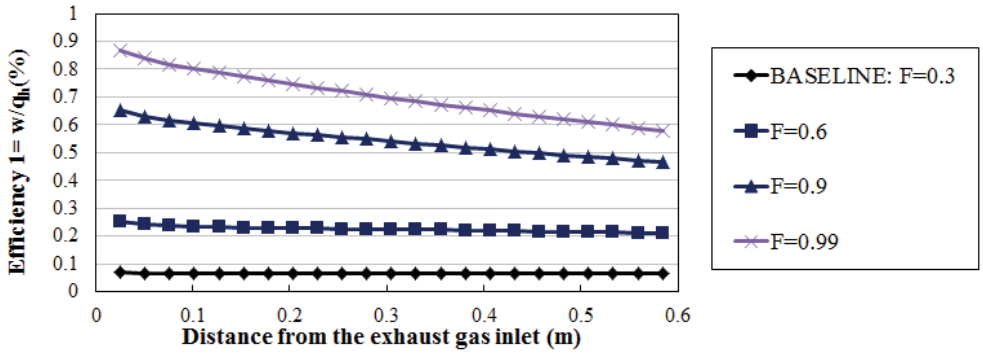

Fig. 24 Effect of TE filling factor on the efficiency of TEG modules along one column of TEG arrays

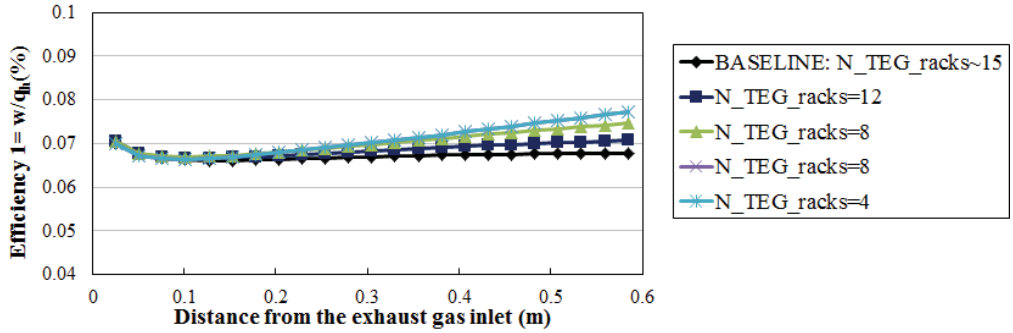

Fig. 25 Effect of SOFC exhaust gas mass flow rate on the efficiency of TEG modules along one column of TEG arrays

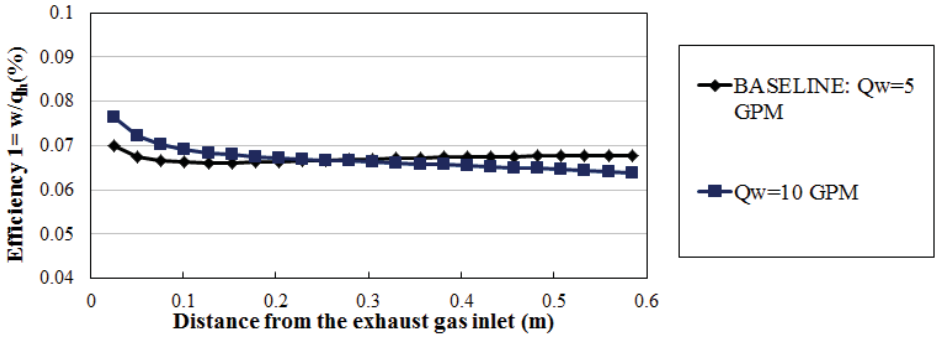

Fig. 26 Effect of rack cooling water mass flow rate on the efficiency of TEG modules along one column of TEG arrays

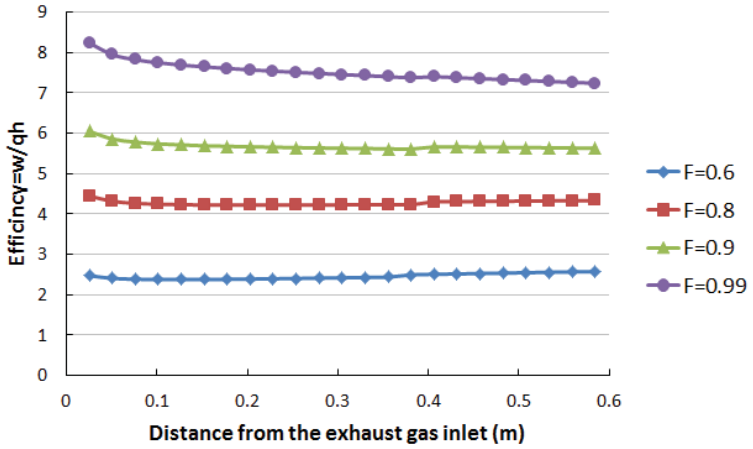

Fig. 27 Efficiency of the optimal TEG modules along one column of TEG array at different filling factors (F)

This is an author-produced, peer-reviewed version of this article. The final, definitive version of this document can be found online at *Proceedings of the Seventeenth InterSociety Conference on Thermal and Thermomechanical Phenomena in Electronic Systems: Itherm 2018*, published by IEEE. Copyright restrictions may apply. doi: 10.1109/ITHERM.2018.8419483

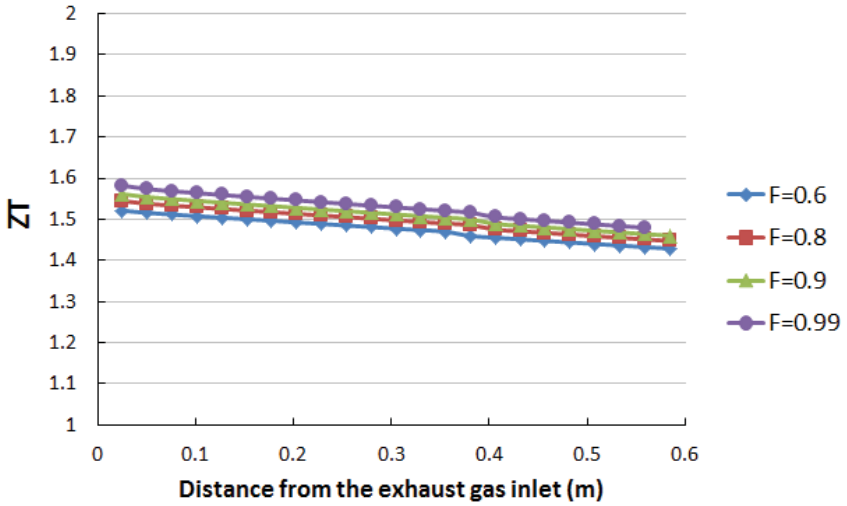

Fig. 28 Figure of Merit (ZT) of the optimal TEG modules along one column of TEG array at different filling factors (F)

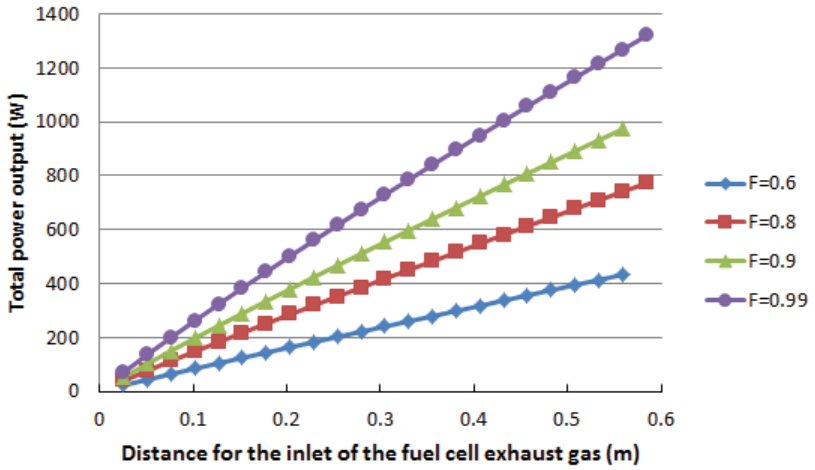

Fig. 29 Total power output of TEG shelf at different filling factors (F)

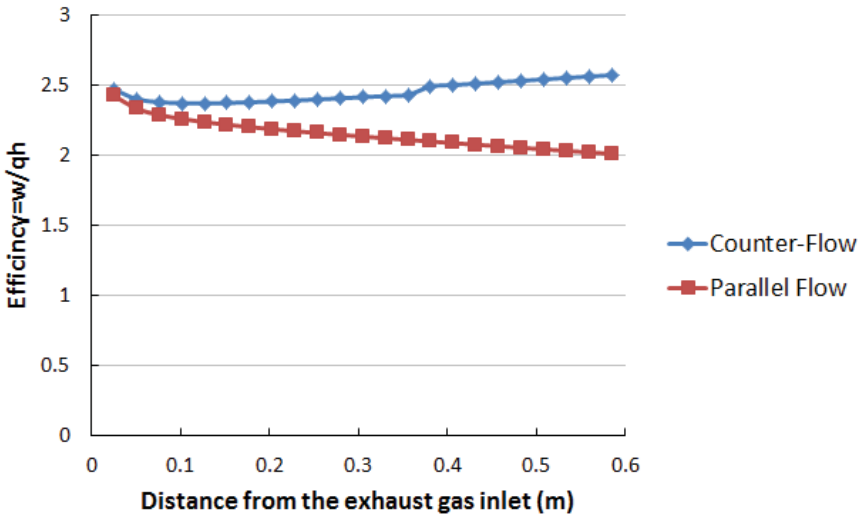

Fig. 30 Comparison between efficiencies in counter-flow and parallel flow configurations under the conditions presented in Table 8 and F=0.6

This is an author-produced, peer-reviewed version of this article. The final, definitive version of this document can be found online at *Proceedings of the Seventeenth InterSociety Conference on Thermal and Thermomechanical Phenomena in Electronic Systems: Itherm 2018*, published by IEEE. Copyright restrictions may apply. doi: 10.1109/ITHERM.2018.8419483

Acknowledgments

This work is supported by Microsoft Inc. Any opinions, findings, and conclusions or recommendations expressed in this material are those of the author(s) and do not necessarily reflect the views of Microsoft, Inc.

References

[1] Martín-González M, Caballero-Calero O, Díaz-Chao P. Nanoengineering thermoelectrics for 21st century: energy harvesting and other trends in the field. Renew Sustain Energy Rev 2013; 24: 288–305.

[2] Roberts RA, Brouwer J. Dynamic Simulation of a Pressurized 220 kW Solid Oxide Fuel Cell-Gas Turbine Hybrid System: Modeled Performance Compared to Measured Results. Journal of Fuel Sci. Tech 2006; 31(1): 18- 25.

[3] Ebrahimi K, Jones GF, Fleischer AS. A review of data center cooling technology, operating conditions and the corresponding low-grade waste heat recovery opportunities. Renew Sust Energ Rev 2014; 31: 622-638.

[4] Aavid Engineering, Inc., EDS#117, Interface Materials, January 1992.

[5] Yazawa K, Shakouri A. Cost-efficiency trade-off and design of thermoelectric power generators. Environ. Sci. Technol 2011; 45(17); 7548-755.

[6] Yazawa K, Koh YR, Shakouri A. Analytical optimization of cost effective thermoelectric generation on top of Rankine cycle. Proceedings of the InterPACK2013, July 16-18, 2013, Burlingame, CA, USA.

[7] Somerford M. Thermal analysis of an integrated masonry unit and a model for the effective R-Value. Master's thesis 2013, Mechanical Engineering Department, Villanova University, Villanova, PA, USA.

[8] Incropera FP, Dewitt DB, Bergman TL, Lavine AS., 2007, Fundamentals of Heat and Mass Transfer, 6th ed., John Wiley & Sons Inc., Printed in USA.

[9] White FM.,2008, Fluid Mechanics, 6th ed. McGraw Hill, New York, NY.

[10] Bejan A, Kraus AD. Heat transfer handbook. John Wiley and Sons Inc.; 2003

[11] Teertstra P, Yovanovich MM, Culham JR, Lemczyk, T. Analytical forced convection modeling of plate fin heat sinks. in Proc. 15th Annu. IEEE Semicon. Thermal Meas. Manag. Symp., San Diego, CA, March 9–11, 1999, pp. 34–41.

[12] Lemmon EW, Huber ML, McLinden MO. NIST reference fluid thermodynamic and transport properties—REFPROP version 8 -User's Guide. National Institute of Standards and Technology Standard Reference Data Program, 2007; Maryland 20899.

[13] Cengel, YA., Boles, MA, 2011, Thermodynamics: An Engineering Approach, 7th ed., McGraw Hill, New York, NY.

[14] Wilke CR. A viscosity equation for gas mixtures. J. Chem. Phys. 1950; 18(4): 517-519.

[15] Cheung H, Bromley LA, Wile CR. Thermal conductivity of gas mixtures. AIChE J 1962; 8(2): 221-228.

[16] Lee S, How to select a heat sink, Electronics Cooling 1 (1) (1995) 10–14.

[17] Lee S, Van Au SS, Moran KP. Constriction/spreading resistance model for electronic packaging. In Proc. 4th ASME/JSME Thermal Engineering Joint Conference, Maui, HI, March 19-24, 1995, Vol. 4; pp. 199-206.

[18] Yazawa K, Shakouri A. Cost performance trade-off in thermoelectric modules with low fractional area coverage, Material Research Society, MRS 2011fall Meeting, (2011).

[19] Copeland D. Optimization of parallel plate heat sinks for forced convection. In Proc 16th Annu. IEEE Semicon. Thermal Meas. Manag. Symp., San Jose, CA, March 21-23, 2000, pp.266-272.

[20] Muzychka YS, Yovanovich MM. Modelling Friction Factors in Non-Circular Ducts for Developing Laminar Flow. In Proc 2nd AIAA Theoretical Fluid Mechanics Meeting, Albuquerque, 15-18 June 1998, AIAA Paper No. 98-2492.

[21] Johnson Matthey Nobel Metals, Iridium Products < http://www.noble.matthey.com/> viewed on November 10, 2015.

[22] AV Bleininge. Technologic Papers of the Bureau of Standards, Issues 1-11, US Dept Commerce and Labor. Washington, DC. Dec 6, 1910.

[23] Thermal conductivity of common alloys in electronics packaging http://www.electronics-cooling.com/ viewed on November 10, 2015.

[24] SM Don, Loss-of-Flow Analysis of an Unfinned, Graded Fuel Meat, LEU Monolithic U-10Mo Fuel Design in Support of the MITR-II Fuel Conversion (MS Thesis), MIT, 2014.

[25] European Copper Institute www.conductivity-app.org/download-alloy-pdf/16, viewed on November10, 2015.

[26] <http://www.electronics-cooling.com/1999/09/the-thermal-conductivity-of-ceramics/> viewed on December 21, 2015.